PNAS RESEARCH ARTICLE | PHYSICS

Observation of two-step melting on a sphere

Navneet Singh[a,1], A. K. Sood[b,c], and Rajesh Ganapathy[c,d,1]

Edited by Erio Tosatti, Scuola Internazionale Superiore di Studi Avanzati, Trieste, Italy; received April 13, 2022; accepted June 10, 2022

Melting in two-dimensional flat space is typically two-step and via the hexatic phase. How melting proceeds on a curved surface, however, is not known. Topology mandates that crystalline particle assemblies on these surfaces harbor a finite density of defects, which itself can be ordered, like the icosahedral ordering of 5-coordinated disclination defects on a sphere. Thus, melting even on a sphere, the simplest closed surface, involves the loss of both crystalline and defect order. Probing the interplay of these two forms of order, however, requires a system in which melting can be performed in situ, and this has not been achieved hitherto. Here, by tuning interparticle interactions in situ, we report an observation of an intermediate hexatic phase during the melting of colloidal crystals on a sphere. Remarkably, we observed a precipitous drop in icosahedral defect order in the hexatic phase where the shear modulus is expected to vanish. Furthermore, unlike in flat space, where disorder can fundamentally alter the nature of the melting process, on the sphere, we observed the signature characteristics of ideal melting. Our findings have profound implications for understanding, for instance, the self-assembly and maturation dynamics of viral capsids and also phase transitions on curved surfaces.

colloids | curved manifolds | 2D melting | phase transitions | BKTHNY

Significance

Unlike in three-dimensional flat space, melting in two dimensions is typically via the hexatic phase—a state with quasi–long-range orientational order but no translational order. However, crystals on curved surfaces harbor a finite number of defects, even in their ground state, to relieve the packing frustration imposed by curving space, and how melting proceeds is unknown. In fact, for crystals on a sphere, these defects are ordered, and melting involves the loss of both crystalline and defect order. Here we show that melting on a sphere is via the hexatic phase and, surprisingly, also unaffected by the presence of curvature-induced defects. Strikingly, defect order vanished in the hexatic window. Our findings can help understand phase transitions on curved surfaces.

The presence of an intermediate hexatic phase in two-dimensional (2D) melting is the smoking gun signaling that the celebrated Berezinskii–Kosterlitz–Thouless–Halperin–Nelson–Young (BKTHNY) mechanism is at play (1–8). In flat space, the hexatic phase—a state characterized by quasi–long-range orientational order but no translational order—has now been found in diverse systems that include electrons on the surface of liquid helium (9), colloidal monolayers (10–13), superconducting vortex lattices (14), and recently, even in films of magnetic skyrmions (15). The nature of melting in 2D flat space, however, is sensitive to the precise form of the interaction potential (8). While for soft particle interactions, melting follows the BKTHNY mechanism and is via two continuous transitions—a crystal-to-hexatic transition by dislocation unbinding, followed by a hexatic-to-liquid transition by disclination unbinding; for hardcore interactions, not only is the hexatic window narrower in comparison, the hexatic–liquid transition is first-order (13, 16). In fact, for dislocation core energies below a threshold value, melting is a first-order transition and is via the proliferation of grain boundaries (4, 6, 17–19). Remarkably, while the nature of 2D flat space melting remains debated even today (7), how melting proceeds on even the simplest closed surface, the sphere, is unknown. Crystalline assemblies of isotropic particles on a sphere typically present twelve 5-coordinated disclination defects, which act as conserved topological charges (20). These disclinations, which are arranged at the vertices of an icosahedron akin to the pentamers on spherical virus capsids (21) or the pentagons on a soccer ball, are bound to linear dislocation arrays forming defect patterns called "scars" for system sizes that exceed a threshold value (22–24). Since defects/disorder profoundly influence the melting mechanisms in flat space (6, 25–28), an early study doubted whether quasi–long-range orientational order can survive in the presence of curvature defects/scars (29). Even while a seminal recent study exploited the icosahedral ordering of defects/scars to show that liquids of soft particles on a sphere freeze into single crystals (30), whether freezing/melting is two-step as posited by BKTHNY remains unknown. Spherical crystals by virtue of their topology are subject to finite-size effects, and these in flat space are known to complicate the determination of phase boundaries (16). In addition, previous 2D flat space melting studies found that while increasing the strength of random disorder destabilizes the crystal phase and broadens the hexatic window (27), when the disorder is itself on a lattice, the crystal is stabilized, but the hexatic window vanishes, and melting is via a first-order transition (28). Thus, for icosahedrally defect-ordered spherical crystals, besides a lack of understanding of how crystalline and defect order collude during melting, it is not evident if the hexatic phase should even intervene.

Micrometer-sized colloids bound to curved oil–aqueous interfaces are a paradigmatic system to probe how the topology of the host surface influences the physics of condensed phases (24, 30–35). A particularly versatile system is charged hydrophobic colloids that

Author affiliations: [a]Chemistry and Physics of Materials Unit, Jawaharlal Nehru Centre for Advanced Scientific Research, Bangalore 560064, India; [b]Department of Physics, Indian Institute of Science, Bangalore 560012, India; [c]International Centre for Materials Science, Jawaharlal Nehru Centre for Advanced Scientific Research, Bangalore 560064, India; and [d]School of Advanced Materials, Jawaharlal Nehru Centre for Advanced Scientific Research, Bangalore 560064, India

Author contributions: N.S. and R.G. designed research; N.S. performed research; N.S. analyzed data; A.K.S. contributed to discussions and provided feedback on the manuscript; R.G. steered research; and N.S. and R.G. wrote the paper.

The authors declare no competing interest.

This article is a PNAS Direct Submission.

See online for related content such as Commentaries.

[1]To whom correspondence may be addressed. Email: navneet22may@gmail.com or rajeshg@jncasr.ac.in.

This article contains supporting information online at https://www.pnas.org/lookup/suppl/doi:10.1073/pnas.2206470119/-/DCSupplemental.

Published August 3, 2022.

are bound to these interfaces due to image charge forces (30, 32, 33, 35). Besides being amenable to single-particle scale imaging of dynamics, the phase behavior of this system is governed by a single dimensionless parameter, $\Gamma = \frac{(\pi\rho)^{3/2}A}{k_B T}$, which is the ratio of electric dipole and thermal energies (30). Here $k_B T$ is the thermal energy, ρ is the number density of particles on the surface, and A is the magnitude of the dipolar pair potential $U(r) \sim \frac{A}{r^3}$, where r is the distance between particles. With this system, however, different phases have hitherto been realized by starting from samples with a different ρ (30, 32, 33, 35). Given that in flat space, the hexatic phase often appears in a narrow range of the control parameter (11–13, 15), the essential prerequisite for detecting the hexatic, if it is at all present, during melting on a sphere is to be able to tune Γ continuously and in situ.

Results

In Situ Melting on a Sphere. We found that introducing trace amounts of sodium hydroxide (NaOH) in a system of charged hydrophobic polymethyl methacrylate (PMMA) colloids bound to the interface of spherical oil droplets in an aqueous phase resulted in melting (*Materials and Methods*). Since ρ remained constant, it is A that decreases upon NaOH addition. This is possibly because of the diffusion of some of the excess hydroxyl radicals from the aqueous into the oil phase resulted in better screening of the colloid charge. Further, the decrease in A is linear (*Materials and Methods* and *SI Appendix*, Figs. S1 and S2), and tuning the NaOH concentration in a narrow window allowed tuning of the melting rate (*SI Appendix*, Table S1). Equipped with this capability to tune Γ in situ, we now dissected the melting process.

The confocal micrographs shown in Fig. 1*A* capture the transition from a visually ordered initial state (Fig. 1 *A*, *Top*) to a disordered final state (Fig. 1 *A*, *Bottom*) for $N = 1{,}538$ particles on a sphere of radius $R = 29$ μm (*SI Appendix*, Fig. S3 and Movie S1). The corresponding Voronoi tessellations of these assemblies, however, are more revealing (Fig. 1*B*). To begin with, the tessellation is typical of a large spherical crystal (Fig. 1 *B*, *Top*) (30); particles maintained their preferred sixfold coordination except at the 12 spatially localized grain boundary scars each with an array of dislocations (pairs of 5- and 7-coordinated particles with a net topological charge of zero) strung to a disclination (5-coordinated particle with topological charge +1). These excess dislocations help screen the disclinations' stress field and are required only when system size exceeds a threshold value, $\frac{R}{a} > 5$, where a is the mean interparticle separation (22, 24). For the system shown in Fig. 1*A*, $\frac{R}{a} \sim 10$ and scars are indeed expected. Once melting is complete, coordination defects are many and are homogeneously distributed in the liquid (Fig. 1 *B*, Bottom).

We confirmed defect-ordering in our spherical crystals through the defect–defect correlation function $g_{DD'}(s)$ (Fig. 1*C*) (29, 36). Here s is the geodesic distance (expressed in radians), and the subscripts D and D' denote the type of disclination considered, either a 5- or a 7-coordinated particle while calculating this quantity. The features seen in $g_{DD'}$ at small s are a consequence of local correlations between defects. However, the two peaks at large s, centered on θ_1 and θ_2 and seen only for large Γ, are due to the icosahedral ordering of the scars (30) (*SI Appendix*, Fig. S5). These defect correlations are lost when the crystal melts and the peaks vanish (small Γ values).

The simple analysis above threw a surprise. In Fig. 1*D*, we plot the peak height of $g_{DD'}(s = \theta_1) = g^1_{DD'}$, a coarse measure of the extent of defect ordering, and the spatiotemporally averaged hexagonal bond-order parameter, $\langle|\psi_6|\rangle = \langle|\psi_6(\mathbf{r}_i, t)|\rangle$, against Γ. Here $\psi_6(\mathbf{r}_i, t) = \frac{1}{N_i}\sum_{j=1}^{N_i} e^{6i\theta_{ij}(t)}$, where N_i is the coordination of particle i located at $\mathbf{r}_i$ at time t and θ_{ij} is the angle made by line joining the centers of particle i and its nearest-neighbor j with respect to an arbitrary reference axis (37). Initially, both $g^1_{DD'}$ and $\langle|\psi_6|\rangle$ decrease, and this decrease is more rapid for the longer-ranged defect correlations. However, intriguingly, in a narrow range of $110 \geq \Gamma \geq 85$, defect ordering melts—$g^1_{DD'}$ drops precipitously, even while the globally averaged crystallinity remains high. In fact $\langle|\psi_6|\rangle > 0.7$—the lower bound often used to detect crystalline order in flat space (Movie S2) (38, 39).

Melting on a Sphere Is Two-Step and via the Hexatic Phase. We gleaned insights into this observation by focusing on how spherical crystals lost their long-ranged translational and orientational order during melting. Unlike in flat space, detecting this order on a curved manifold is hampered because the basis vectors themselves now vary in space, making parallel vector transport path-dependent (40). However, by exploiting the broken symmetry of the defect-ordered state to define a global reference axis, long-ranged correlations can be uncovered. Following ref. 30, we found the orientation of the icosahedron whose vertices overlapped best with the defects and then projected the particles onto the faces of this icosahedron as shown in Fig. 1*E* (*SI Appendix*, Fig. S7). Unfolding this icosahedron onto a plane revealed the underlying structure of these particle assemblies shown for three representative Γ values in Fig. 1 *F*–*H*. Here particles are colored according to their local orientation, $\theta'_i = \arg(\psi'_{6,i})/6$, which spans from $0° - 60°$ due to the hexagonal symmetry (13), and $\psi'_{6,i}$ is the icosahedrally referenced bond order parameter of particle i (Movie S3). For the largest Γ, the spherical crystal is a single crystal; orientational and positional order display global coherence—θ'_i is nearly a constant except at the vertices, and the structure factor, $S(q)$, shows well-defined bright spots with hexagonal symmetry (*SI Appendix*, Fig. S8). The presence of only short-ranged isotropic order, characteristic of the liquid state, for the smallest Γ is apparent in Fig. 1*H*. For intermediate Γ (Fig. 1*G*), however, while orientational order appears reasonably long-ranged, the peaks in $S(q)$ are azimuthally broadened, which is suggestive of a hexatic phase (*SI Appendix*, Fig. S9) (12, 19, 41). Interestingly, this Γ value lies in the window where we observed a steep drop in $g^1_{DD'}$ (Fig. 1*D*).

A hallmark of the BKTHNY mechanism of melting (1–5) is that positional correlations disappear before orientational ones (12, 13, 15), and in between, the latter is quasi–long-ranged in both space and time, a signature of the hexatic phase (11). To this end, we tracked the evolution of positional order through the modified Lindemann parameter, $\gamma_L(t) \approx \frac{\langle \Delta s_{ij}(t)^2\rangle}{2a^2}$ (*SI Appendix*) (12), and of orientation by the icosahedrally referenced space and time correlations of ψ'_6, these being $g'_6(s) = \langle \psi'_6(\mathbf{r_i})\, \psi'^*_6(\mathbf{r_j})\rangle_{R\cos^{-1}(\mathbf{r_i}.\mathbf{r_j}/R^2)=s}$ (30) and $g'_6(\tau) = \langle \psi'_{6,i}(t)\psi'^*_{6,i}(t')\rangle_{t-t'=\tau}$, respectively (*SI Appendix*). Here $\Delta s_{ij}(t)$ is the relative geodesic displacement of nearest-neighbor particles i and j. While for $\Gamma \geq 110$, $\gamma_L(t)$ remained constant in time with particles only rattling about their lattice positions, for smaller Γ, it diverged at long times as $\gamma_L(t) \propto t^\beta$ (Fig. 2*A*) with $\beta \to 1$ in the liquid (Fig. 2 *D*, *Top*, and *SI Appendix*, Fig. S12 for various N). We identified the Γ where β began to increase ($\Gamma \approx 110$) as the crystal–hexatic boundary, Γ_{CH} (Fig. 2 *D*, *Top*) (13).

Fig. 2 *B* and *C* show $g'_6(s)$ and $g'_6(t)$, respectively. Both quantities remained flat for the crystal ($\Gamma \geq 110$) and decayed exponentially for $\Gamma \leq 85$, which we identified as the onset of the liquid state (*SI Appendix*, Figs. S13 and S14 for various N) (13, 15). Importantly, for $110 > \Gamma > 83$, orientational correlations were

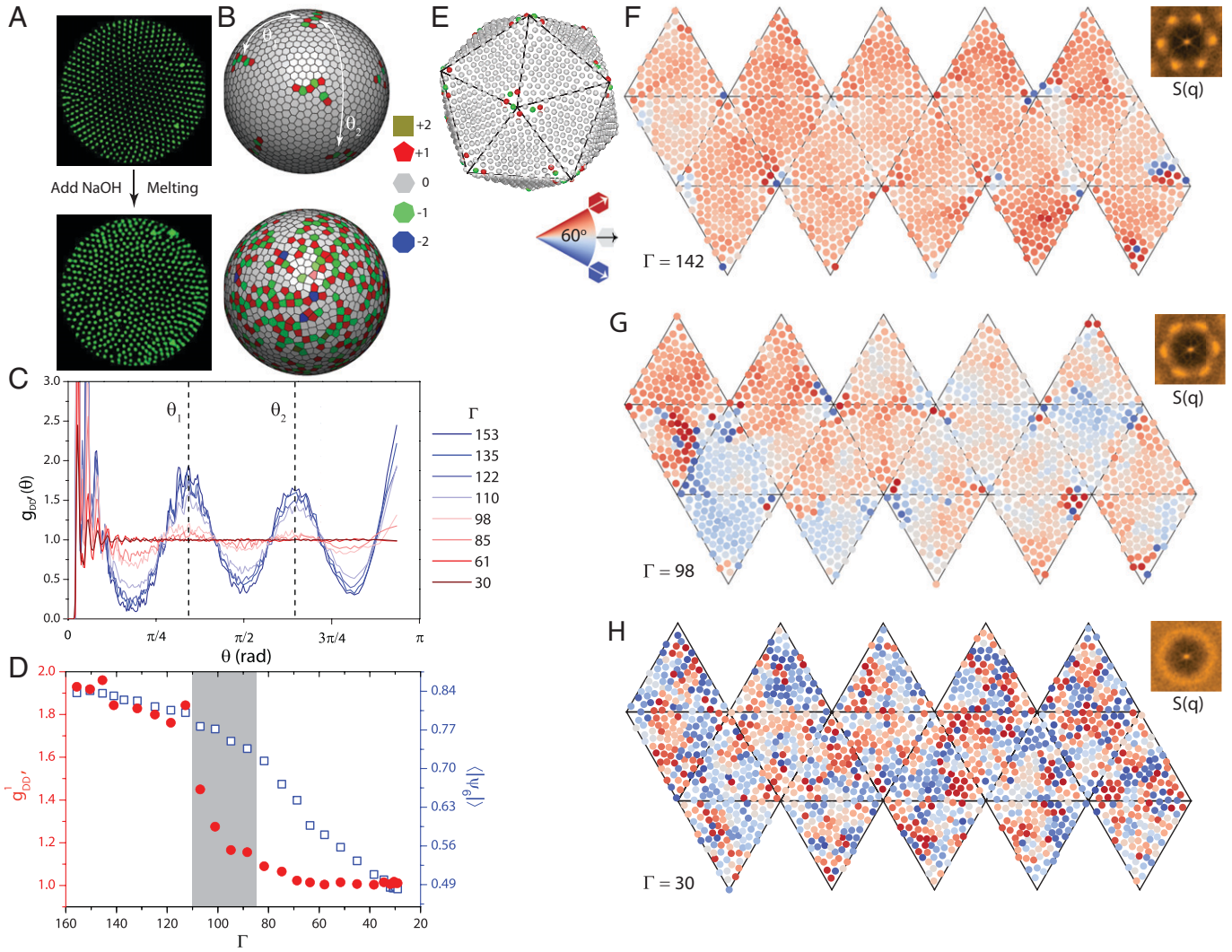

Fig. 1. Melting of crystalline and icosahedral defect order on a sphere. (*A*) Reconstructed confocal micrographs of charged colloids of radius 0.75 μm (shown in green) on the surface of a sphere, before (*Top*) and after (*Bottom*) the addition of NaOH. (*B*) The corresponding Voronoi tessellations of these particle packings. For the spherical crystal, the defects are localized (*Top*), whereas for the liquid (*Bottom*), defects are spatially homogeneous. The polygons are colored according to their local coordination, and their corresponding topological charge is also indicated. (*C*) Defect–defect pair correlation function $g_{DD'}(\theta)$ versus geodesic distance s (expressed in radians) for various Γ values. At high Γ, the peaks of $g_{DD'}(\theta)$ at θ_1 and θ_2 are due to the icosahedral ordering of defects, while at low Γ, these peaks vanish. (*D*) The peak amplitude of $g_{DD'}(\theta=\theta_1)=g^1_{DD'}$ and the average magnitude of the bond-orientational order parameter, $\langle|\psi_6|\rangle$, versus Γ. $g^1_{DD'}$, alone, decays rapidly at intermediate Γ (gray-shaded region). (*E*) The projection of particles onto a reference icosahedron that is oriented such that its vertices coincides with the positions of the topological defects. Here particles shown in red and green are 5- and 7-coordinated, respectively, while those shown in gray have sixfold coordination. (*F–H*) Unfolding of the fitted icosahedron on to a plane at $\Gamma = 142$ (*F*), $\Gamma = 98$ (*G*), and $\Gamma = 30$ (*H*). The particles are colored according to their local orientation θ_i'. (*Right*) The structure factors $S(q)$ of the unfolded structures. Long-ranged orientational and translational order is present for $\Gamma = 142$, while there is a lack of both of these for $\Gamma = 30$. For $\Gamma = 98$, orientational order appears to be medium-ranged, and the peaks in $S(q)$ are azimuthally broadened—a telltale signature of the hexatic phase.

quasi–long-ranged, evidenced by the algebraic decay in $g_6'(s) \propto s^{-\eta_6}$ and $g_6'(t) \propto t^{-\eta_6/2}$, confirming the existence of the hexatic phase. Further, by reducing the system size to gain access to faster 3D imaging speeds, we also directly observed the unbinding of spontaneously generated dislocation pairs into free dislocations predicted to occur in the hexatic regime (Fig. 2*E*) (42). BKTHNY theory also predicts a universal value of $\eta_6 \to 1/4$ on nearing the hexatic–liquid transition, which, here, occurs at $\Gamma_{HL} \approx 83$ (13, 15). Notably, the increase in β precedes η_6 for all N, suggesting that melting of spherical crystals is two-step (Fig. 2 *D*, *Top* and *Middle*, and *SI Appendix*, Fig. S15). In further support of this observation, the increase in the number density of excess dislocations was at Γ_{CH}, while that in disclinations was at Γ_{HL} (*SI Appendix*, Fig. S16 for various N) (12). We note that we did not observe the proliferation of grain boundaries in the vicinity of Γ_{CH} for any N (*SI Appendix*, Fig. S10), suggesting that the grain boundary melting mechanism is not at play here (4, 6, 17–19).

Loss of Icosahedral Defect Order in the Hexatic Phase. Since elastic interactions between curvature defects mediate their ordering (22, 23), we anticipated that the loss of this order (Fig. 1*D*) occurred entirely in the hexatic phase, which lacks translational order and hence also a shear and Young's modulus (4, 5, 42) (*SI Appendix*, Fig. S18). To verify this, we quantified defect ordering through an order parameter sensitive to icosahedral symmetry (30, 43), this being the rotationally invariant 3D, three-body bond-orientational order parameter, $\widetilde{W_6}$, which is defined as

$$\widetilde{W_6} = -\frac{\sqrt{4{,}999}}{11} \sum_{m_1,m_2,m_3=-6}^{6} \begin{pmatrix} 6 & 6 & 6 \\ m_1 & m_2 & m_3 \end{pmatrix} \frac{\rho_{6m_1}\rho_{6m_2}\rho_{6m_3}}{(\sum_m |\rho_{6m}|^2)^{3/2}}. \quad [1]$$

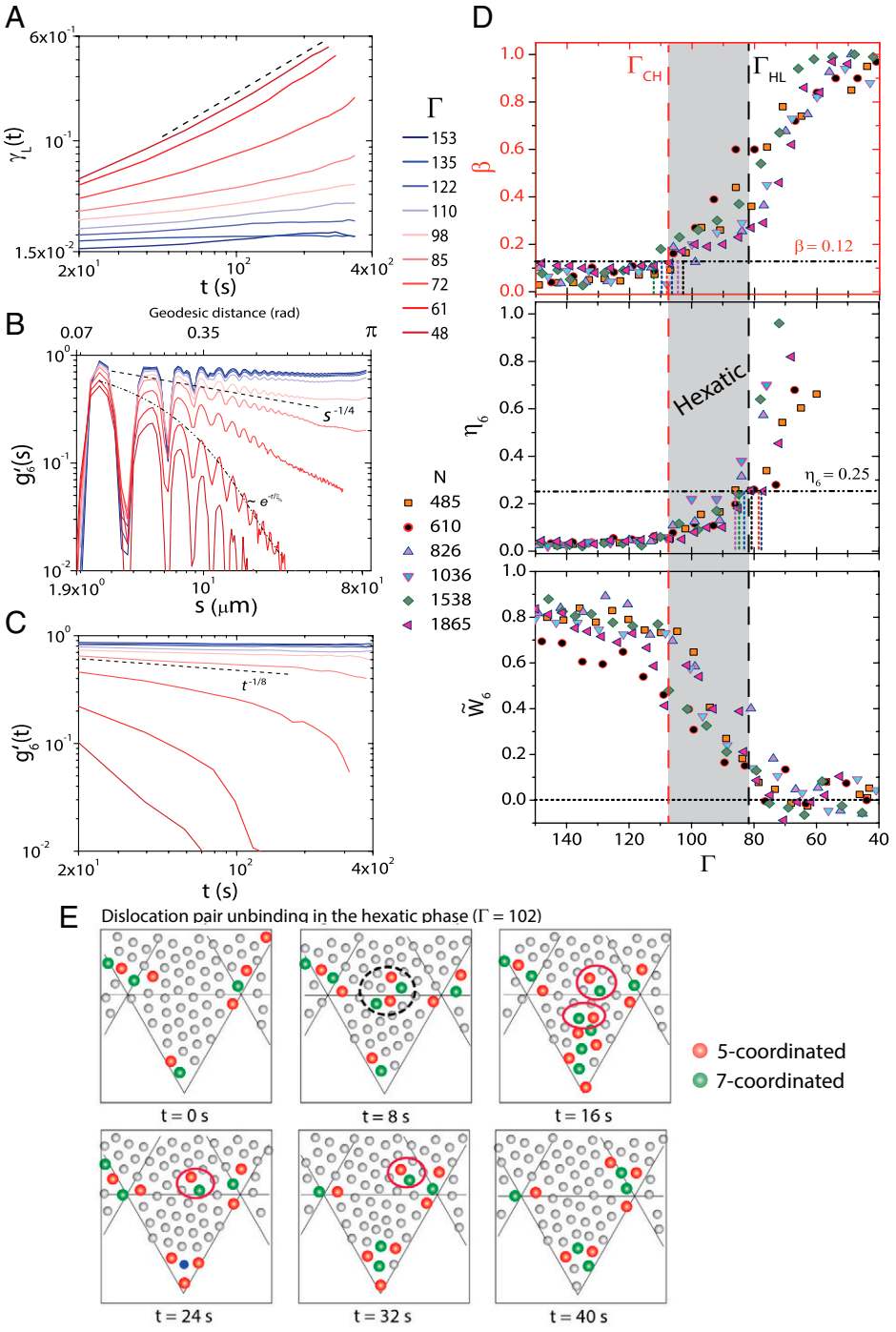

Fig. 2. Evidence for the hexatic phase and identifying its role in the loss of defect order. (*A*) The modified Lindemann parameter, $\gamma_L(t)$, for various Γ. $\gamma_L(t)$ is flat for the crystal and scales as $\sim t^{\beta}$, at long times, with decrease in Γ. The black dashed line is a guide to the eye and has slope 1. (*B* and *C*) The icosahedrally referenced orientational space and time correlation functions, $g_6'(s)$ and $g_6'(t)$, respectively, for various Γ. The black dash-dotted curve is an exponential fit to the upper envelope of the data. The critical power law decay exponent $\eta_6 \to 1/4$ as predicted by BKTHNY theory is shown by the black dashed line. In *C*, the dashed line has an exponent $-\eta_6/2 \to -1/8$, and this value is reached on nearing the hexatic–liquid boundary. (*D*) (*Top* and *Middle*) The Γ dependence of the power law exponents β and η_6 for different system sizes, *N*, respectively. The vertical dotted lines in *Top* and *Middle* indicate the crystal–hexatic, Γ_{CH}, and hexatic–liquid, Γ_{HL}, transitions for each *N*, respectively. (*Bottom*) The rotationally invariant 3D, three-body bond-orientational order parameter, $\widetilde{W_6}$, which is sensitive to the icosahedral ordering of defects, for various *N*. The gray shaded region is the hexatic window. (*E*) Time evolution of a dislocation pair unbinding in the hexatic phase for $N = 485$ particles. The black dash-dotted and solid red ovals show the bound dislocation pair and free dislocations, respectively.

Here the first term in the summand is the Wigner-3j symbol and $\rho_{6m} = \sqrt{4\pi}\sum_i Y_{6m}(\theta_i, \phi_i)$ with Y_{6m} being the sixth-order spherical harmonic, and θ_i and ϕ_i are the coordinates of defect i. For a regular icosahedron, $\widetilde{W_6}$ takes the maximum value of 1. $\widetilde{W_6}$ is large ($\sim$0.8) and constant for $\Gamma \geq \Gamma_{CH}$ and is around zero for $\Gamma \leq \Gamma_{HL}$, with the drop lying almost entirely in the hexatic window for all N (Fig. 2 *D*, Bottom).

Curvature-Induced Defects Do Not Interfere with Melting. Our fast imaging experiments also helped investigate if grain boundary scars had a role during melting. For instance, in flat space, grain

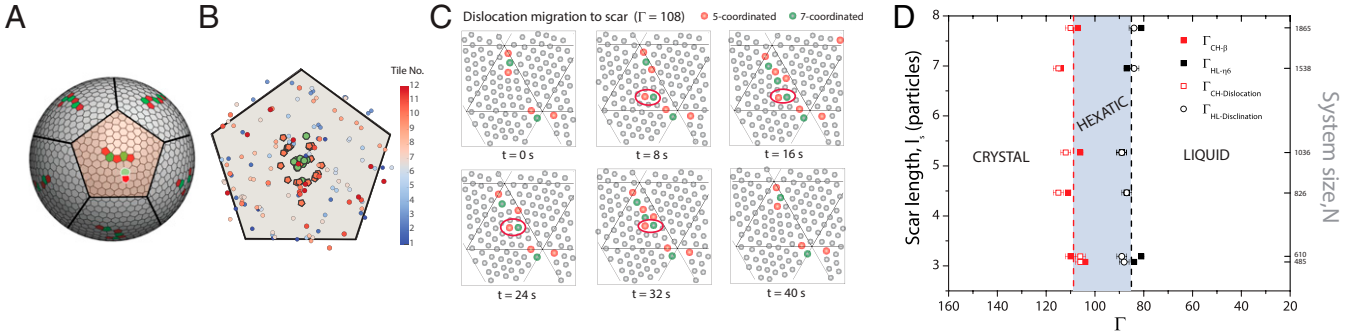

Fig. 3. Hexatic regime is robust to the presence of scars. (*A*) The Voronoi tessellation of the sphere with scar centers as sites. The Voronoi cells are pentagons due to the icosahedral ordering of the scars. The shaded pentagon also shows a dislocation located away from the scar. (*B*) The 12 pentagonal tiles superimposed. The first appearance of a dislocation in each tile is marked (circles) and is colored according to the tile number. The red pentagons and the green heptagons in the center of the tile are the 12 scars. (*C*) Dislocation (marked by red oval) migration to and annihilation at a scar in the hexatic regime. Only the initial part of the hexatic phase ($110 > \Gamma \geq 95$) was considered for this analysis since scars lost their individual identities on nearing the hexatic–liquid boundary due to the proliferation of defects (*SI Appendix*, Fig. S19). (*D*) The crystal–hexatic (red symbols) and hexatic–liquid (black symbols) phase boundaries for various system sizes *N* obtained through two measures: the first from the translational and orientational correlation functions and the second from the number of topological defects. $\Gamma_{CH-\beta}$ corresponds to the Γ where $\beta > 0.1$, and $\Gamma_{HL-\eta 6}$ is the Γ where η_6 crosses 0.25 (Fig. 2 *D*, *Top* and *Middle* panels). $\Gamma_{CH-\text{Dislocations}}$ and $\Gamma_{HL-\text{Disclinations}}$ correspond to the Γ where the number of dislocations and disclinations begin to increase, respectively. The dashed lines are the phase boundaries obtained from linear fits to data that were obtained by averaging the two different measures. The right axis is a label for each data point denoting the system size. The scar length l_s increases with *N* (*SI Appendix*, Figs. S22 and S23), but the location of the hexatic window remains unchanged.

boundaries act as sources or sinks for vacancies and dislocations (44, 45). However, we found that crossing the crystal–hexatic boundary, the primary source for excess free dislocations was not scars but rather the unbinding of dislocations in bulk. We quantified this observation by using scar centers as sites for first carrying out a Voronoi tessellation of the sphere surface and then marking the position of the dislocations the first time they appeared in each tile (Fig. 3*A*). These tiles are pentagons due to the icosahedral ordering of scars. Superimposing these tiles helped visualize where dislocations appeared on the entire sphere surface, and Fig. 3*B* clearly shows this is random and not exclusively near scars. There was nevertheless a tendency for dislocations to migrate to and annihilate at scars (Fig. 3*C*), and this is in line with earlier studies that found that the anisotropic stress field of scars draws defects toward them (*SI Appendix*, Fig. S20 for quantitative analysis of dislocation migration) (33, 46).

While dislocation annihilation at scars led to a small increase in their length (*SI Appendix*, Fig. S21), this did not appear to influence the melting process significantly. Since the number of excess dislocations per scar scales linearly with the system size, a straightforward way to probe the role of the scar length, l_s, on the melting behavior is to simply increase the total number of particles in the spherical crystals (*SI Appendix*, Figs. S22 and S23). Fig. 3*D* shows the experimentally determined phase boundaries for various N (Fig. 2*D* and *SI Appendix*, Fig. S16). We see that l_s more than doubles in length over the range of N studied, but strikingly, the Γ values of the crystal–hexatic and the hexatic–liquid transitions remain more or less unchanged.

Conclusions. In flat space, premelting of thick polycrystalline films (>4 monolayers) often initiates at grain boundaries (26). On reducing the film thickness, premelting effects weaken (47), but even for monolayer films, frozen-in grain boundaries increase defect formation probabilities and thus enhance melting (48). Our observation that grain boundary scars, irrespective of their length, largely remain passive players and leave the hexatic window unscathed is, therefore, quite surprising. This is all the more so, given an earlier study that found that these scars, just like grain boundaries in flat space, are spatially correlated with regions of high mobility (30). Clearly, defects whose sole purpose is to relieve the stress induced by curving space are less intrusive than their flat space siblings in the physics of melting/freezing. We anticipate an exciting future ahead wherein it may now be possible to import concepts from flat space to understand phase transitions in condensed matter systems on complex topologies (49–51).

Materials and Methods

Experiments were performed using fluorescently labeled sterically stabilized PMMA (Poly methylmethacrylate) colloids of radius $r = 0.75$ μm suspended in an oil mixture (cyclohexyl bromide [75% vol/vol] and decalin [25% vol/vol]), whose refractive index and density are precisely matched with those of the particles. The suspension was then added to an aqueous mixture containing glycerol, DMSO (dimethyl sulfoxide), and water (8:1:1 vol/vol) (for more details, see *SI Appendix*). Emulsion droplets (oil in aqueous medium) with a radius ranging from 10 to 200 μm were formed via manual shaking. The samples are then loaded in an open cylindrical cell and sealed from above with an oil seal. All the glasswares used are cleaned by dipping for 30 min in a 2.5 M solution of NaOH and then drying at 70 °C in an oven for 12 h. The PMMA particles are known to become charged in oil (cyclohexyl bromide and decalin) due to the partial dissociation of **HBr** component of cyclohexyl bromide into $\mathbf{H^+}$ and $\mathbf{Br^-}$ (52). These charged PMMA particles bind to the oil–aqueous interface due to the formation of the image charges of opposite signs in the aqueous phase, without absorbing to the interface (52, 53). The PMMA colloids interact via a dipolar pair potential, $U(r) = \frac{A}{r^3}$, where A is the magnitude of the dipolar pair potential, and r is the distance between particles (30).

We found that adding 2 μL of sodium hydroxide (NaOH 100 mM) to this system resulted in a monotonic decrease of magnitude of the dipolar pair potential, A (*SI Appendix*, Fig. S1). This is because the ions diffuse from the aqueous mixture to the emulsion droplets until a balance is reached. The ion diffusion process helps screen the colloid charge and allows tuning Γ, which in turn results in melting of the crystal (*SI Appendix*, Fig. S3).

Using a Leica SP8-II confocal microscope (63X oil immersion objective, N.A. 1.4), we followed the melting dynamics of the colloidal crystals. The 3D stacks were captured at frame rate spanning from 7 to 25 s per stack. ImageJ and MATLAB were used to process and render the images. We have used standard MATLAB algorithms to find the center-of-mass coordinates of the colloidal particles (54). All other analyses were done using custom-written codes in MATLAB (for more details, see *SI Appendix*).

Data Availability. All study data are included in the article and/or supporting information. Raw data are available upon request from corresponding author.

ACKNOWLEDGMENTS. N.S. thanks the Council for Scientific and Industrial Research, India, for a Senior Research Fellowship. A.K.S. thanks Department of Science and Technology (DST), Government of India, for a Year of Science Fellowship. R.G. thanks DST-Nanomission grant SR/NM/TP-25/2016 and DST-SwarnaJayanti Fellowship for financial support.

1. J. M. Kosterlitz, D. J. Thouless, Ordering, metastability and phase transitions in two-dimensional systems. *J. Phys. C Solid State Phys.* **6**, 1181 (1973).
2. B. Halperin, D. R. Nelson, Theory of two-dimensional melting. *Phys. Rev. Lett.* **41**, 121 (1978).
3. A. Young, Melting and the vector coulomb gas in two dimensions. *Phys. Rev. B Condens. Matter* **19**, 1855 (1979).
4. K. J. Strandburg, Two-dimensional melting. *Rev. Mod. Phys.* **60**, 161 (1988).
5. G. Venkataraman, D. Sahoo, Melting in two dimensions–The current status. *Pramana* **24**, 317–350 (1985).
6. J. Dash, History of the search for continuous melting. *Rev. Mod. Phys.* **71**, 1737 (1999).
7. J. M. Kosterlitz, Kosterlitz-Thouless physics: A review of key issues. *Rep. Prog. Phys.* **79**, 026001 (2016).
8. V. N. Ryzhov, E. Tareyeva, Y. D. Fomin, E. N. Tsiok, Berezinskii–Kosterlitz–Thouless transition and two-dimensional melting. *Phys. Uspekhi* **60**, 857 (2017).
9. M. A. Stan, A. J. Dahm, Two-dimensional melting: Electrons on helium. *Phys. Rev. B Condens. Matter* **40**, 8995–9005 (1989).
10. C. A. Murray, D. Van Winkle, Experimental observation of two-stage melting in a classical two-dimensional screened Coulomb system. *Phys. Rev. Lett.* **58**, 1200–1203 (1987).
11. K. Zahn, R. Lenke, G. Maret, Two-stage melting of paramagnetic colloidal crystals in two dimensions. *Phys. Rev. Lett.* **82**, 2721 (1999).
12. Y. Han, N. Y. Ha, A. M. Alsayed, A. G. Yodh, Melting of two-dimensional tunable-diameter colloidal crystals. *Phys. Rev. E Stat. Nonlin. Soft Matter Phys.* **77**, 041406 (2008).
13. A. L. Thorneywork, J. L. Abbott, D. G. A. L. Aarts, R. P. A. Dullens, Two-dimensional melting of colloidal hard spheres. *Phys. Rev. Lett.* **118**, 158001 (2017).
14. I. Guillamón *et al.*, Direct observation of melting in a two-dimensional superconducting vortex lattice. *Nat. Phys.* **5**, 651–655 (2009).
15. P. Huang *et al.*, Melting of a skyrmion lattice to a skyrmion liquid via a hexatic phase. *Nat. Nanotechnol.* **15**, 761–767 (2020).
16. E. P. Bernard, W. Krauth, Two-step melting in two dimensions: First-order liquid-hexatic transition. *Phys. Rev. Lett.* **107**, 155704 (2011).
17. S. Chui, Grain-boundary theory of melting in two dimensions. *Phys. Rev. Lett.* **48**, 933 (1982).
18. K. J. Strandburg, Crossover from a hexatic phase to a single first-order transition in a Laplacian-roughening model for two-dimensional melting. *Phys. Rev. B Condens. Matter* **34**, 3536–3539 (1986).
19. A. H. Marcus, S. A. Rice, Observations of first-order liquid-to-hexatic and hexatic-to-solid phase transitions in a confined colloid suspension. *Phys. Rev. Lett.* **77**, 2577–2580 (1996).
20. M. J. Bowick, L. Giomi, Two-dimensional matter: Order, curvature and defects. *Adv. Phys.* **58**, 449–563 (2009).
21. R. F. Bruinsma, G. J. L. Wuite, W. H. Roos, Physics of viral dynamics. *Nat. Rev. Phys.* **3**, 76–91 (2021).
22. M. J. Bowick, D. R. Nelson, A. Travesset, Interacting topological defects on frozen topographies. *Phys. Rev. B Condens. Matter Mater. Phys.* **62**, 8738 (2000).
23. M. Bowick, A. Cacciuto, D. R. Nelson, A. Travesset, Crystalline order on a sphere and the generalized Thomson problem. *Phys. Rev. Lett.* **89**, 185502 (2002).
24. A. R. Bausch *et al.*, Grain boundary scars and spherical crystallography. *Science* **299**, 1716–1718 (2003).
25. L. Pauchard, D. Bonn, J. Meunier, Dislocation-mediated melting of a two-dimensional crystal. *Nature* **384**, 145–147 (1996).
26. A. M. Alsayed, M. F. Islam, J. Zhang, P. J. Collings, A. G. Yodh, Premelting at defects within bulk colloidal crystals. *Science* **309**, 1207–1210 (2005).
27. S. Deutschländer, T. Horn, H. Löwen, G. Maret, P. Keim, Two-dimensional melting under quenched disorder. *Phys. Rev. Lett.* **111**, 098301 (2013).
28. W. Qi, A. P. Gantapara, M. Dijkstra, Two-stage melting induced by dislocations and grain boundaries in monolayers of hard spheres. *Soft Matter* **10**, 5449–5457 (2014).
29. S. P. Giarritta, M. Ferrario, P. Giaquinta, Statistical geometry of hard particles on a sphere: Analysis of defects at high density. *Physica A Stat. Mech. Appl.* **201**, 649–665 (1993).
30. R. E. Guerra, C. P. Kelleher, A. D. Hollingsworth, P. M. Chaikin, Freezing on a sphere. *Nature* **554**, 346–350 (2018).
31. P. Lipowsky, M. J. Bowick, J. H. Meinke, D. R. Nelson, A. R. Bausch, Direct visualization of dislocation dynamics in grain-boundary scars. *Nat. Mater.* **4**, 407–411 (2005).
32. W. T. Irvine, V. Vitelli, P. M. Chaikin, Pleats in crystals on curved surfaces. *Nature* **468**, 947–951 (2010).
33. W. T. Irvine, M. J. Bowick, P. M. Chaikin, Fractionalization of interstitials in curved colloidal crystals. *Nat. Mater.* **11**, 948–951 (2012).
34. G. Meng, J. Paulose, D. R. Nelson, V. N. Manoharan, Elastic instability of a crystal growing on a curved surface. *Science* **343**, 634–637 (2014).
35. N. Singh, A. K. Sood, R. Ganapathy, Cooperatively rearranging regions change shape near the mode-coupling crossover for colloidal liquids on a sphere. *Nat. Commun.* **11**, 4967 (2020).
36. S. P. Giarritta, M. Ferrario, P. Giaquinta, Statistical geometry of hard particles on a sphere. *Physica A Stat. Mech. Appl.* **187**, 456–474 (1992).
37. D. R. Nelson, Order, frustration, and defects in liquids and glasses. *Phys. Rev. B Condens. Matter* **28**, 5515 (1983).
38. Y. L. Wu, D. Derks, A. van Blaaderen, A. Imhof, Melting and crystallization of colloidal hard-sphere suspensions under shear. *Proc. Natl. Acad. Sci. U.S.A.* **106**, 10564–10569 (2009).
39. K. H. Nagamanasa, S. Gokhale, R. Ganapathy, A. K. Sood, Confined glassy dynamics at grain boundaries in colloidal crystals. *Proc. Natl. Acad. Sci. U.S.A.* **108**, 11323–11326 (2011).
40. G. F. T. del Castillo, *3-D Spinors, Spin-Weighted Functions and Their Applications* (Springer Science & Business Media, 2003), **vol. 32**.
41. G. Aeppli, R. Bruinsma, Hexatic order and liquid density fluctuations. *Phys. Rev. Lett.* **53**, 2133–2136 (1984).
42. U. Gasser, C. Eisenmann, G. Maret, P. Keim, Melting of crystals in two dimensions. *ChemPhysChem* **11**, 963–970 (2010).
43. P. J. Steinhardt, D. R. Nelson, M. Ronchetti, Bond-orientational order in liquids and glasses. *Phys. Rev. B Condens. Matter* **28**, 784 (1983).
44. H. Gleiter, Grain boundaries as point defect sources or sinks–Diffusional creep. *Acta Metall.* **27**, 187–192 (1979).
45. I. J. Beyerlein, M. J. Demkowicz, A. Misra, B. Uberuaga, Defect-interface interactions. *Prog. Mater. Sci.* **74**, 125–210 (2015).
46. M. Bowick, H. Shin, A. Travesset, Dynamics and instabilities of defects in two-dimensional crystals on curved backgrounds. *Phys. Rev. E Stat. Nonlin. Soft Matter Phys.* **75**, 021404 (2007).
47. Y. Peng, Z. Wang, A. M. Alsayed, A. G. Yodh, Y. Han, Melting of colloidal crystal films. *Phys. Rev. Lett.* **104**, 205703 (2010).
48. S. Deutschländer, C. Boitard, G. Maret, P. Keim, Grain-boundary-induced melting in quenched polycrystalline monolayers. *Phys. Rev. E Stat. Nonlin. Soft Matter Phys.* **92**, 060302 (2015).
49. J. Tempere, I. F. Silvera, J. T. Devreese, Multielectron bubbles in helium as a paradigm for studying electrons on surfaces with curvature. *Surf. Sci. Rep.* **62**, 159–217 (2007).
50. A. Tononi, L. Salasnich, Bose-Einstein condensation on the surface of a sphere. *Phys. Rev. Lett.* **123**, 160403 (2019).
51. V. P. Kravchuk *et al.*, Topologically stable magnetization states on a spherical shell: Curvature-stabilized skyrmions. *Phys. Rev. B* **94**, 144402 (2016).
52. M. Leunissen, "Manipulating Colloids with Charges & Electric Fields," PhD thesis, Utrecht University, Utrecht, The Netherlands (2007).
53. M. E. Leunissen, A. van Blaaderen, A. D. Hollingsworth, M. T. Sullivan, P. M. Chaikin, Electrostatics at the oil-water interface, stability, and order in emulsions and colloids. *Proc. Natl. Acad. Sci. U.S.A.* **104**, 2585–2590 (2007).
54. J. C. Crocker, D. G. Grier, Methods of digital video microscopy for colloidal studies. *J. Colloid Interface Sci.* **179**, 298–310 (1996).